Published in final edited form as:
Adv Ther (Weinh). 2021 September ; 4(9): . doi:10.1002/adtp.202100033.

Optimization of microbubble-based DNA vaccination with low-frequency ultrasound for enhanced cancer immunotherapy

Nisi Zhang[1], **Josquin Foiret**[1], **Azadeh Kheirolomoom**[1], **Pei Liu**[1], **Yi Feng**[1], **Spencer Tumbale**[1], **Marina Raie**[1], **Bo Wu**[1], **James Wang**[1], **Brett Z. Fite**[1], **Zhifei Dai**[2], **Katherine W. Ferrara**[1,*]

[1]Department of Radiology, Stanford University, Palo Alto, CA, USA

[2]Department of Engineering, Peking University, Beijing, China

Abstract

Immunotherapy is an important cancer treatment strategy; nevertheless, the lack of robust immune cell infiltration in the tumor microenvironment remains a factor in limiting patient response rates. *In vivo* gene delivery protocols can amplify immune responses and sensitize tumors to immunotherapies, yet non-viral transfection methods often sacrifice transduction efficiency for improved safety tolerance. To improve transduction efficiency, we optimized a strategy employing low ultrasound transmission frequency-induced bubble oscillation to introduce plasmids into tumor cells. Differential centrifugation isolated size-specific microbubbles. The diameter of the small microbubble population was 1.27 ± 0.89 μm and that of larger population was 4.23 ± 2.27 μm. Upon *in vitro* insonation with the larger microbubble population, 29.7% of cancer cells were transfected with DNA plasmids, higher than that with smaller microbubbles (18.9%, $P < 0.05$) or positive control treatments with a commercial transfection reagent (12%, $P < 0.01$). After 48 h, gene expression increased more than two-fold in tumors treated with large, as compared with small, microbubbles. Furthermore, the immune response, including tumor infiltration of CD8$^+$ T cells and F4/80$^+$ macrophages, was enhanced. We believe that this safe and efficacious method can improve preclinical procedures and outcomes for DNA vaccines in cancer immunotherapy in the future.

Keywords

Microbubble; Ultrasound; Cancer; Gene transfection; Immunotherapy

1 Introduction

Immunotherapy can lead to efficient tumor-specific immune responses by activating the immune system. In current clinical practice, these therapies include immune checkpoint

---

[*] Corresponding author kwferrar@stanford.edu.

Author contributions

N.Z., A.K., Y.F., K.W.F. designed research; N.Z., J.F., P.L., S.K.T., M.R., B.W. performed cell and animal study; N.Z., J.F. and B.Z.F. performed ultrasound imaging. N.Z., J.W., and K.W.F. analyzed the data and wrote the paper. Z.D. contributed to the manuscript.

Conflict of Interest

The authors declare no conflict of interest.

inhibitors [1]. However, these inhibitors, such as anti-programmed death 1 antibody (aPD-1), have only achieved limited antitumor efficacy in clinical trials, and can be accompanied by severe adverse events [2]. In poorly immunogenic tumors, checkpoint inhibitors are often combined with additional interventions [3]. DNA vaccination has been extensively tested as an approach to generate or rescue endogenous tumor-reactive T cells [4], and can be administered repeatedly for long-term protection. To enhance antitumor immunity, cytokines are used to improve tumor antigen presentation or enhance T cell activity against cancer cells [5], but it is difficult to induce the desired immune response using traditional methods because of the high metabolic rate of cytokines, low gene transfer efficiency or transgene expression level and bio-safety concerns [6].

Therapeutic genes are transferred using either viral or non-viral vectors [7]. Viral vectors are typically retroviral, adenoviral or adeno-associated vectors [8]. Despite their efficacy, viral vectors have limitations. Although stable gene expression is achieved via viral integration mechanisms, the integration into the host genome can lead to unexpected mutagenesis [9]. With high immunogenicity, viruses also carry the risk of recombination, reversion to virulence, and subsequent pathogenesis. Non-viral vectors have significant advantages over viral vectors due to their favorable properties, including lack of immunogenicity, low toxicity, and potential for tissue specificity [10], but their gene transfer efficiency is not satisfactory [11]. Our previous study [12] demonstrated that local co-administration of a plasmid and targeted microbubbles (TMBs), coupled with low-transmission frequency ultrasound, provides a relatively safe and effective method to produce an anticancer cytokine, and to consequently promote T cell inflammation at both treated and distant tumor sites for improved efficacy.

Low-frequency ultrasound irradiation can produce a mechanical perturbation of the cell membrane, facilitating the uptake of molecules in the vicinity of the cavitation [13]. Microbubbles (MBs) are used as ultrasound contrast agents, carriers for targeted drug delivery, or vehicles for metabolic gas transport [14], and importantly, can lower the threshold for cavitation [15]. Cavitation promotes the formation of fluid microjets, shockwaves, streaming, and cavitation forces, which in turn give rise to shear stresses on the cellular membrane and vascular barrier [16]. The oscillating pressure field induced by ultrasound wave impinging upon the MB surface creates stable compression and expansion of the gas core at lower acoustic pressures (hundreds of kPa) than that required in the absence of MBs [17]. The collapse of these MBs generates small transient pores in the cell membrane and enhances temporary membrane permeabilization, a process known as sonoporation [18, 19]. The size of pores formed in the cell membrane can be a limiting factor for delivery of macromolecules, such as gene constructs, into cells [20, 21]. Since bubbles decrease in size after inertial cavitation [22], we hypothesize that larger MBs combined with low frequency ultrasound will be more effective for cell membrane disruption.

For improved performance in DNA vaccination, MBs require precise size control. Matching the resonant frequency can maximize MB expansion, generate greater acoustic radiation force, and enhance adhesion of targeted molecules and drug delivery [23]. In experimental studies and computational predictions [24], the resonance frequency decreased nonlinearly with larger MB equilibrium diameter. Moreover, differential centrifugation can be a useful approach to generate narrow distributions of MBs at specific diameters for biomedical applications [25], and facilitates study of the surface properties and efficacy of varied MB size populations in gene transfection.

Herein, we report the protocols and results of an optimized MB-based DNA transfection strategy. Granulocyte-macrophage colony stimulating factor (GM-CSF) is a potent cytokine activator of antigen presenting cells [26], such as dendritic cells (DCs), and can regulate macrophage numbers and function [27]. GM-CSF secreting cancer vaccines have been reported to break self-tolerance and induce massive accumulation of DCs at the inoculated site and in turn activating tumor specific T cells and macrophages to induce an anti-tumor immune response [26]. Therefore, the combination of PD-1 blockade with GM-CSF production in cancer cells can be an effective approach to improve the anti-tumor immune response [28]. Naked DNA vaccines are easy and inexpensive to produce and store [29], and plasmids are thermally stable [30]. Therefore, in this study, we selected naked GM-CSF plasmids (pGM-CSF), explored the transfection efficiency *in vitro* and *in vivo*, and evaluated the anticancer efficacy of immunotherapy in tumor-bearing mice (Figure 1). We show that the optimized MB-based transfection enhanced the transfer efficiency and pGM-CSF vaccines combined with aPD-1 induced a remarkable antitumor immune effect in both treated and distant tumors.

2 Results

2.1 Characterization of MBs

To target murine breast cancer cells (NDL cells), MBs were conjugated with the anti-mouse CD326 antibody, also called epithelial cell adhesion molecule (EpCAM) antibody. Preparation of EpCAM antibody-targeted MB suspension by shaking a lipid mixture resulted in a polydisperse suspension of ~ 10^9 to 10^{10} particles mL^{-1} (Table S1). The freshly generated bubble suspension contained two TMB populations characterized by a bimodal size distribution curve based on dynamic light scattering (DLS) measurements (Figure 2A). Differential centrifugation was applied to isolate the two narrowly-dispersed fractions into their corresponding size ranges. The diameter of the small bubble (s-TMB) population was 1.27 ± 0.89 μm and that of the larger population (l-TMB) was 4.23 ± 2.27 μm (Figure 2A, Table S1). Given that the tumor vasculature is composed of vessels with a diameter up to 200 μm and capillaries ranging from 5 to 10 μm [31], these bubbles were appropriate for tumor perfusion. TMBs with various sizes also have been observed using optical microscopy (Figure 2A).

When incubated with cancer cells, an average of 15.13 ± 2.03 small or 8.20 ± 1.90 large TMBs were adherent to each cell, respectively (Figure 2B). A custom-made experimental system was established for ultrasound treatment and guidance (Figure S1). *In vitro* passive cavitation detection (PCD) was used to monitor the cavitation activity by recording and quantifying ultra-harmonic components and broadband energy in the spectrum. Ultra-harmonics were detected for ~ 2 and more than 4 s with s-TMB- and l-TMB-targeted cells, respectively (Figure 2C). The extended oscillation of large MBs resulted from the lower expansion ratio. Based on the Marmottant model, insonation with a center frequency of 250 kHz and 500 kPa of acoustic pressure generated an expansion ratio of 40 and 10 fold for s-TMB and l-TMB, respectively (Figure 2D) [32]. The expansion ratio threshold for inertial cavitation ranges from 2.3 to 3.5 [33] and therefore the parameters are expected to result in inertial cavitation. Our previous study [12] confirmed that TMBs do not fragment at the same rate as nontargeted MBs when attached to cells.

2.2 *In vitro* study of plasmid delivery

To investigate the effect of MB-enhanced sonoporation on DNA transfection, we used Cy5-labeled plasmid luciferase (Cy5-pLuc) as a marker for gene delivery in experiments conducted with cells attached to coverslips. Confocal imaging showed that intracellular transport of Cy5-pLuc induced by TMBs through membrane pores increased the total Cy5 fluorescence intensity in the cytoplasm or nuclei (Figure 3A). We estimated the size of pores from the measured fluorescence intensity of CellMask. Larger pores generated by l-TMBs and ultrasound (US) were measured from the relative fluorescence intensity for DAPI, calcium green AM, CellMask and Cy5 by displaying two-dimensional graphs of the intensity values along a dashed line in Image J (Figure 3B, Figure S2). The plasma membrane signal decreased in the cells treated with TMBs. In the absence of TMBs, Cy5-pLuc was not detected in cells.

TMB-insonation produced a different cytosolic pattern of distribution after insonation. In the group with s-TMB treatment, Cy5-pLuc remained near cell nuclei but lacked nuclear co-localization. With l-TMB insonation, Cy5 and DAPI spectra overlapped, indicating that more plasmids were internalized and entered the cell nucleus after enhanced sonoporation.

2.3 *In vitro* study of gene transfection

Since TMB-enhanced sonoporation was able to improve Cy5-pLuc plasmid delivery, we further investigated its efficacy in gene transfection with green fluorescent protein plasmid (pGFP). *In vitro* transfection experiments were conducted for cells in suspension. pGFP was delivered via sonoporation with a center frequency of 250 kHz for 3 min. 48 h after US treatment, the percentage of GFP^+ cells was visualized by confocal microscopy (Figure 4A) and quantified using flow cytometry (Figure 4B). For the samples treated with pGFP + TMB + US, the fraction of GFP^+ live cells was 29.70% with l-TMBs, higher than that with s-TMBs (18.93%, $P < 0.05$) or positive control treatments with the transfection reagent JetPrime (12%, $P < 0.01$) (Figure 4C). Conversely, in all samples treated without US, the GFP signal was similar to that of non-treatment control (NTC) group. The same US conditions also increased GM-CSF production with TMB sonoporation. In addition to pGFP, we measured the cellular uptake and expression of pGM-CSF by quantifying GM-CSF production using ELISA. We observed a 1.3-fold increase in GM-CSF secretion in cells treated with pGM-CSF + l-TMB + US, compared to that in the pGM-CSF + s-TMB + US ($P < 0.01$) or JetPrime ($P < 0.01$) cohorts (Figure 4D).

2.4 *In Vivo* Reporter Gene Transfection

In vivo reporter gene transfection experiments were performed in the bilateral NDL murine breast cancer model, using plasmids encoding optical reporter genes (pLuc and pGFP). The delivery of pLuc enabled direct visualization via bioluminescence imaging *in vivo*, while pGFP facilitated quantitation of transfection via ex vivo fluorescence imaging of tumors. To achieve localized plasmid accumulation, plasmid administration via sonoporation was carried out by intratumoral (i.t.) injection of a mixture of TMBs and pLuc/pGFP (injected volume was 25 μL). As reported in several studies [34, 35], the distance between the bubble and cell affects cavitation efficacy, and i.t. injection can enhance MB binding to tumor cells. Following i.t. injection, wide tumor distribution of TMBs was visualized with contrast pulse sequence nonlinear imaging (red dashed circle) (Figure 5A, Figure S3). MBs are hypothesized to travel through tissues after i.t. injection due to their flexible structure and the convection generated from injection. Ultrasound imaging at the tumor site confirmed a high concentration of MBs throughout the tumor (Figure 5A, Figure S3).

Following insonation using the *in vitro* optimized parameters, ultrasound imaging subsequently confirmed the complete destruction of TMBs in the tumors (Figure 5B). PCD was used to monitor the *in vivo* cavitation activity by recording and quantifying ultra-harmonic components and broadband energy in the spectrum. During *in vivo* transfection, discrete harmonics and wideband echoes were detected for about 20 s in the tumors treated with s-TMBs, and for more than 40 s in l-TMB group. MB cavitation was observed for a longer time during *the in vivo* study as compared with the *in vitro* study. MB oscillation is restricted within the tissue stroma and likely enhances MB longevity.

Bioluminescence imaging at 24 h tracked luciferase gene expression. Luciferase expression was absent in NTC mice (Figure 5C), and detected in mice treated with or without TMBs using 500 kPa. Expression was enhanced 5.8-fold further in mice treated with l-TMBs compared with no TMBs ($P < 0.01$), and was 2-fold greater than in mice treated with s-TMB ($P < 0.05$) (Figure 5D). This is consistent with the in vitro data that l-TMBs exhibit higher transfection efficiency than s-TMBs. Fluorescence ex vivo measurement of pGFP transfection also showed results similar to the pLuc expression level. The GFP intensity was 2.7-fold higher in l-TMB group than in the s-TMB group (Figure S4). The result showed that TMB-enhanced sonoporation facilitated the introduction of pLuc and pGFP into tumors, and could be optimized for transfection with other plasmids.

2.5 *In vivo* DNA vaccination for immunotherapy

GM-CSF transfection in tumor cells was shown to induce durable anti-tumor immunity based on an adaptive immune response [36], and we therefore hypothesized that TMB-enhanced sonoporation would further improve the efficacy of GM-CSF transfection. To test this hypothesis, we developed a treatment regime where GM-CSF plasmid delivery was augmented by our TMB sonoporation protocol and combined with checkpoint inhibitor aPD-1. The immune response was evaluated using immunohistochemistry (IHC). Plasmid delivery via sonoporation was carried out by intratumoral (i.t.) injection of a mixture of TMBs with pGM-CSF into one tumor within the bilateral tumor models. We sought to further enhance and amplify the immune response and generate a systemic immune response by transfecting the tumor with pGM-CSF. Since the tumor’s checkpoint inhibitory mechanisms limit immune cell activity, the transfection protocol incorporated the intraperitoneal (i.p.) administration of an anti-PD-1 (aPD-1) checkpoint inhibitor. As shown in Figure 6A, aPD-1 was initially administered 3 days prior to the pGM-CSF transfection, and the tumors were collected 3 days post vaccination and assayed using hematoxylin and eosin (H&E) staining and CD8 and F4/80 immunohistochemistry (IHC). The results established that the sustained TMB oscillations are capable of debulking the tumor and reducing its viability (Figure 6B, Figure S5). Insonation with l-TMBs led to mechanical damage to tumor cells [37]. Extensive damage and reduced tumor viability were visualized in H&E slices, indicating that l-TMBs increased the oscillation amplitude compared to s-TMBs.

On IHC collected 7 days post aPD-1 treatment, immune cell infiltration (F4/80$^+$ macrophages and CD8$^+$ T cells) increased in both the directly-treated tumors and the distant tumors, compared to all other controls as quantified using ImageJ. CD8$^+$ T cell recruitment in the directly-treated aPD-1 +pGM-CSF +l-TMB +US tumors increased more than 3.5-fold compared to the pGM-CSF +l-TMB +US, aPD-1 +l-TMB +US and aPD-1 +pGM-CSF +s-TMB +US groups (all $P < 0.01$), and more than 18-fold compared to NTC, aPD-1 only, and l-TMB +US groups (all $P < 0.01$) (Figure 6C, S6). Distant tumor T cell recruitment following aPD-1 +pGM-CSF +l-TMB +US treatment was enhanced at least 1.8-fold compared to the l-TMB +US ($P < 0.01$), pGM-CSF +l-TMB +US ($P < 0.01$), aPD-1 +l-TMB +US ($P < 0.01$) and aPD-1 +pGM-CSF +s-TMB +US ($P < 0.05$) groups, and more than 20-fold compared to NTC and aPD-1 groups (Figure 6D, S6). However, the enhancement of macrophage infiltration was not significant compared to l-TMB +US, pGM-CSF +l-TMB +US and aPD-1 +l-TMB +US groups. F4/80$^+$ macrophages were also enhanced in the directly-treated tumors with aPD-1 +pGM-CSF +l-TMB +US treatment; ~40% of cells were macrophages, a significant increase of 3.6-, 3.6- and1.5-fold, compared to NTC ($P < 0.01$), aPD-1 only ($P < 0.01$) and aPD-1 +pGM-CSF +s-TMB +US ($P < 0.05$), respectively (Figure 6E, Figure S7).

The effect on the distant tumor is also evident, with macrophages representing ~22% of the cells in the distant tumor following treatment with aPD-1 +pGM-CSF +l-TMB +US, a 7.4-, 2.7-, 1.8-, 1.4-, 1.3- and 1.2-fold increase compared to the NTC ($P < 0.01$), aPD-1-only ($P < 0.01$), l-TMB +US ($P < 0.01$), pGM-CSF +l-TMB +US ($P < 0.01$), aPD-1 +l-TMB +US ($P < 0.05$) and aPD-1 +pGM-CSF +s-TMB +US ($P < 0.05$) groups, respectively (Figure 6F, FigureS7). The enhanced recruitment of immune cells demonstrated the enhanced efficiency of pGM-CSF transfection and cytokine production, showing the potential to induce an immune response for cancer therapy.

2.6 *In vivo* evaluation of anticancer efficacy

The IHC results motivated us to hypothesize that TMB sonoporation enhanced pGM-CSF transfection would result in significant tumor growth reduction when combined with aPD-1. Here, aPD-1 was first administered 3 days prior to and a day following pGM-CSF transfection with sonoporation, and the combinational treatment was executed twice (full regimen is presented in Figure 7A). Immediately after sonoporation, a significant reduction in tumor growth was detected in both treated and distant tumors in the full combinational treatment with l-TMB, compared to control treatments (Figure 7B). With the full large TMB treatment, tumor volume in the treated tumors was reduced 2 weeks after the first US treatment, and the treated and distant tumors were each smaller than aPD-1 + pGM-CSF + s-TMB +US-treated cohorts. Moreover, survival was enhanced with aPD-1 + pGM-CSF +

l-TMB + US compared to all of the other cohorts. Only in the l-TMB-combined treatment group was complete regression observed after more than 20 days. The distant tumor volume was also reduced with aPD-1 + pGM-CSF + l-TMB + US treatment as compared to all control groups (Figure 7C). Meanwhile, the body weight steadily increased after treatment, and there was no evident difference between groups after 25 days (Figure S8). Extensive damage and reduced tumor viability were visualized in H&E slices after l-TMB+US treatment suggesting that l-TMB oscillation led to larger oscillation compared to s-TMBs (Figure 7D, Figure S9).

Treatment efficacy was also evaluated by using Ki67 IHC. Ki67 is an important indicator for cell proliferation and is considered as a prognostic marker in breast cancer [38]. Ki67$^+$ cancer cells were suppressed in the directly-treated tumor with aPD-1 +pGM-CSF +l-TMB +US treatment; only ~5% of cells were Ki67$^+$, 7.5-, 3.2-, 3.5-, 2.9-, 1.6- and 1.8-fold lower than the NTC, aPD-1-only, l-TMB +US, pGM-CSF +l-TMB +US, aPD-1 +l-TMB +US and aPD-1 +pGM-CSF +s-TMB +US groups, respectively (Figure 7E). In the distant tumor ~6% of cells are Ki67$^+$ following treatment with aPD-1 +pGM-CSF +l-TMB +US, a 5.3-, 2.3-, 2.4-, 2.2- and 1.3-fold decrease compared to the NTC, aPD-1-only, l-TMB +US, pGM-CSF +l-TMB +US and aPD-1 +l-TMB +US groups, respectively (Figure 7F, Figure S10).

3 Discussion

DNA vaccines have been applied in various cancer clinical trials; however, a major obstacle in tumor cell vaccine technology is inefficient stimulation of an anti-tumor immune response. The lack of potency of some DNA vaccines highlighted the challenges encountered in efforts to translate efficacy observed in preclinical models into clinical reality. MBs in combination with ultrasound have the potential to enhance local drug and gene delivery. We chose to co-inject MBs and plasmids with the following rationale. Cationic MBs carrying plasmids can potentially protect naked plasmids from nuclease-induced degradation and are commonly used to enhance gene transfection. Nevertheless, cationic materials can adhere to syringes and other surfaces and cationic materials can be toxic. Furthermore, plasmids may not fully separate from the cationic lipids after insonation [39]. Alternatively, antibodies provide specific binding to tumor cells.

This work developed a rational strategy to improve gene transfection by taking advantage of size-selected MBs. We co-injected the plasmids with MBs and insonified locally (rather than using systemic delivery). Compared to our previous work, there are three primary improvements. First, by carefully selecting TMBs with specific sizes and densities, the percentage of cells transfected and the cytokine secretion levels was further increased. By characterizing and correlating the sonoporation effect with DNA delivery and transfer outcome, we found that inertial MB cavitation generated the highest rate of membrane disruption and intracellular delivery. Based on MB activity, we studied pore formation in plasma membranes to improve gene internalization and transfection. Second, we implemented an integrated sonoporation system using low-frequency focused ultrasound with real-time imaging guidance and cavitation detection. Ultrasound contrast-agent imaging facilitated observation of bubble perfusion, biodistribution, and destruction in tumors during insonation. PCD tracked the cavitation activity and confirmed sonoporation after ultrasound application. Further development of transducers that allow for co-registered imaging and 250 kHz transfection will be important for future clinical applications.

Lastly, by using pGM-CSF combined with the checkpoint inhibitor, aPD-1, the recruitment of antitumor immune response was enhanced as a result of sonoporation. With the blockade of the checkpoint receptor, PD-1, the recruitment of macrophages and tumor-reactive T cells increased. GM-CSF is known to induce macrophage activation by binding to the heteromeric GM-CSF receptor [40], and upregulating DC maturation, which leads to T cell infiltration in tumors [41]. Compared with either monotherapy, we found that in the combinational immunotherapy, plasmid delivery and transfection recruited immune cells to the tumor microenvironment in both treated and distant sites, and thus suppressed tumor progression. In the future, many potential plasmids can be incorporated within this therapeutic protocol.

Clinical translation of MB-based approaches for gene transfer remains a challenge, yet this work has demonstrated the potential to improve the methodology. Here, the use of l-TMBs enhanced oscillation during low-frequency insonation, as observed using PCD. The expansion ratio of l-TMBs was ~10, while s-TMBs were estimated to expand over 40 times and were more rapidly destroyed. Discrete harmonics and wideband echoes were detected *in vivo* in the spectrum for more than 40 s in the l-TMB group, double that in s-TMB. As a result of this inertial cavitation, tumor debulking in s-TMB and l-TMB groups was further confirmed using IHC. Due to the prolonged oscillation, sonoporation and pore size were enhanced by the larger MBs. Sonoporation has been reported to disrupt actin cytoskeleton organization and induce nuclear contraction [34, 42]. We found that the plasmid co-localized with the nucleus with l-TMB cavitation, possibly as a result of nuclear contraction. Transfection was enhanced 5.8-fold in mice treated with l-TMBs compared with no TMB, and 2-fold compared to mice treated with s-TMBs. Therefore, we verified that the delivery of plasmids was more efficient when larger pores were likely formed through persistent oscillations of l-TMBs. Our results suggest that rational optimization of sonoporation based on MB dynamics improves gene transfection efficiency and enhance the anticancer immune response.

Overall, we confirmed that MB-based DNA transfection facilitates gene delivery and tumor debulking and enhances the efficacy of immunotherapy. The delivery of plasmid DNA in this study is minimally invasive and easily reproducible. In the future, immunostimulants can be combined to improve therapeutic outcomes in animal models, and ultimately translated to patients.

4 Experimental section

4.1 Materials

All solutions were prepared using filtered, 18.2 MΩ deionized water (Direct-Q, Millipore, Billerica, MA). The gas used to form MBs was perfluorobutane (C_4F_{10}) at 99 wt% purity obtained from FluoroMed (Round Rock, TX). 1,2-Distearoyl-sn-glycero-3-phosphocholine (DSPC), 1,2-distearoyl-sn-glycero-3-phosphoethanolamine-N-[methoxy(polyethyleneglycol)-2000] (DSPE-PEG2000), DSPE-PEG2000-biotin were purchased from Avanti Polar Lipids (Alabaster, AL), and dissolved in chloroform (Sigma-

Aldrich) for storage. Streptavidin was purchased from Sigma-Aldrich and dissolved in deionized water. Biotin-conjugated anti-mouse CD326 antibody was used (clone G8.8; BioLegend, San Diego, CA). The reporter vector luciferase plasmid, pLuc, encodes for the luciferase2 gene driven by a ubiquitin promoter in a pGLA4 backbone (Promega, Madison, WI, USA). The green fluorescent protein plasmid, pGFP, encodes for the optical reporter gene GFP under the control of the cytomegalovirus promoter in a lentiviral (pCCLc) backbone (pCCL-CMV-GFP, produced by the Stem Cell Program Vector Core at the UC Davis Medical Center). The GM-CSF vector, encoding the murine granulocyte macrophage colony-stimulating factor gene, was purchased from GenScript USA Inc. (Piscataway, NJ, Clone ID: OMu22682C, Vector: pcDNA3.1(+)-P2A-eGFP). The plasmids were amplified and purified referring to standard procedures.

4.2 MB preparation and isolation

Biotinylated MBs used in the experiments were prepared as reported previously [12]. MBs were conjugated with EpCAM antibody. The TMBs were suspended in phosphate buffered saline without calcium and magnesium (PBS−/−). Between each step, we washed the streptavidin and EpCAM antibody three times with PBS−/− for TMB purification. Differential centrifugation was used to isolate size-selected MBs based on their migration in a centrifugal field. To calculate the Relative Centrifuge Force (RCF) of the centrifugal field, the initial size distribution and concentration of MBs were measured with an Accusizer 770A (Particle Sizing Systems, Port Richey, FL), which measures particle size and count via single light obscuration. We mixed the bubbles and removed 2 μL of the bubble solution and added it into the stirring system (filled with 50 mL DI water). The concentration, dilution constant and the size population were measured automatically. Particle sizing showed a distribution ranging from the lower limit of resolution, ~0.5 μm, to greater than 15 μm diameter. Following Stokes' law [43], the equation for the rise velocity of a buoyant particle relative to the bulk fluid under creeping flow conditions was used as follows:

$$v = \frac{2}{9}\frac{(\rho_{mb} - \rho_0)}{\mu} g R^2 , \; \frac{\mu}{\mu_0} = 1 + 2.5c + 7.6c^2$$

where R is the MB radius, g is the gravitational acceleration measured in RCF, ρ_{mb} and ρ_0 are the mass density of MB and fluid, respectively. μ is the effective viscosity of the MB suspension, and is calculated using Batchelor and Greene's [44] correlation. c is the total the MB volume fraction (c<1), c^2 represents the bulk stress behavior, and μ_0 is the uniform viscosity of fluid. It is assumed that a bubble moves under the influence of hydrodynamic stresses at the bubble surface only. The effects of Brownian motion of particles are included in the analysis.

The equations above were used to calculate the centrifugal field (in RCF) for a given initial size distribution and time length. Volume fraction was assumed to be constant over the entire column, and acceleration/deceleration effects were neglected in the experiment.

The pre-segmented TMBs were diluted in 1 mL PBS−/−, and isolated by performing centrifugation cycles at 50 RCF for 1 min. The infranatant consisting of 1-2 μm diameter

MBs was saved in another syringe, while the bubble cake was re-dispersed in 1 mL PBS−/− for more centrifugation cycles. These cycles were repeated about 10 times until the infranatant was no longer turbid, indicating complete separation of l-TMBs in bubble cake. The infranatant collected from the isolation was centrifuged at 300 RCF for 3 min for one cycle. The final bubble cake was re-dispersed to a 200 μL of PBS−/−. The size distribution and concentration of s-TMBs and l-TMBs were measured with an Accusizer 770A.

4.3 Simulations for MB expansion ratio

The numerical simulations were performed using the modified Marmottant model [45] to estimate the radial oscillations of MBs with different radius, while taking the effects of liquid compressibility, the shell, and the surrounding tissue into account, as described in previous study [46]. All numerical evaluations were performed in MATLAB R2018a (Mathworks, Natick, MA). A clean gas MB oscillating at a center frequency of 250 kHz was simulated to predict the expansion ratio. The surface tension of the initial MB radius was set to that of saline (0.074 N/m). Shell surface dilatational viscosity was 2.4×10^{-9} kg/s, and elastic compression modulus was 0.55 N/m [47]. The simulations of s-TMB (radius is 0.5 μm) and l-TMB (radius is 2 μm) were performed at the center frequency of 250 kHz [32].

4.4 Cell Culture

An NDL tumor cell line was used in this study. NDL was originated from the overexpression of the ErbB2/neu proto-oncogene [48] and was gifted from the lab of Alexander Borowsky (University of California, Davis, CA). NDL breast cancer cell line was implanted in FVB/N mice. This line is PD-L1 positive and responds to check point inhibitors. Due to the immunogenicity and PD-L1 expression, the NDL cell line serves as an appropriate model for evaluating immunotherapies that involve PD-L1 blockade and immune response activation. Cells were cultured in Dulbecco’s modified Eagle’s medium (DMEM, high glucose, supplemented with 10% fetal bovine serum and 1% penicillin-streptomycin) at 37°C in a humidified 5% CO_2 incubator until their assay using confocal laser microscopic imaging, flow cytometry or Enzyme Linked Immunosorbent Assay (ELISA). For *in vitro* study, cells were grown in cell culture flasks until more than 85% confluent on the day of the experiment.

4.5 Ultrasound treatment

The 250-kHz spherically focused single-element transducer (H-115, Sonic Concepts, Bothell, WA) was placed at the bottom of a degassed water tank facing upwards and aligned to focus at each cell sample. The focal depth of the transducer was 45 mm. Cells or tumors were exposed to sine-wave ultrasound-bursts of 1000 cycles at a 30-Hz pulse repetition frequency (PRF) (duty cycle of 12%) for a total duration of 3 min. The peak negative pressure (PNP) generated in the region of interest was 500 kPa. MB oscillations *in vitro* were monitored by passive cavitation detection (PCD) using an unfocused and single-element transducer at a frequency of 2.25 MHz (V204-RM, Panametrics). The PCD transducer was aligned to the focus of the therapeutic 250-kHz transducer. MB distribution and destruction in tumors were monitored by real-time ultrasound imaging in contrast mode and PCD using a CL15-7 ultrasound transducer probe (128 elements, 0.18 mm pitch, Philips/ATL). Received radio frequency (RF) data were displayed and post processed by using a programmable ultrasound system Vantage 256 (Verasonics, Kirkland, WA).

4.6 Confocal laser microscopy

For the plasmid delivery study, 10^5 adherent cells on 12-mm coverslips in 24-well plates were used, and pLuc was labeled by using Label IT Nucleic Acid Labeling Kit with Cy5 (Mirus Bio LLC). The medium was replaced with 300 μL PBS +/+, and TMBs were added to the well at a ratio of 15 s-TMBs or 7 l-TMBs per cell. After incubation for 40 minutes at room temperature (RT) on a shaker at 200 rounds per minute (rpm), the Cy5-pLuc (10 ug) was added, and degassed PBS+/+ was supplemented to a total volume of 300 μL to each sample. The samples were incubated at RT for another 40 minutes prior to the ultrasound treatment. For the Cy5-pLuc transfection, 3 groups were tested: 1) Cy5-pLuc +US, 2) Cy5-pLuc + s-TMB + US, 3) Cy5-pLuc + l-TMB + US. After ultrasound treatment, the samples were mixed well for 5 minutes at RT on a shaker at 200 rpm. Following the sonoporation, cells were washed with PBS+/+ at RT, and stained with Calcium green AM (#20501, AAT Bioquest), CellMask Orange Plasma membrane stain (#C10045, ThermoFisher Scientific) and 4',6-diamidino-2-phenylindole (DAPI, Sigma-Aldrich) and the coverslips were mounted on clean glass slides. Confocal laser microscopy images were obtained with a ×63 oil-immersion lens (Multiphoton Microscope Leica TCS SP8 MP) to investigate the cellular distribution and localization of the plasmids. Calcium green AM: Ex = 506 nm, Em = 531 nm; CellMask: Ex = 554 nm, Em = 567 nm; DAPI: Ex = 358 nm, Em = 461 nm; Cy5: Ex = 633 nm, Em = 655 nm. All fluorescent dyes were used following the manufacturer’s instructions.

4.7 Flow cytometry

For the pGFP transfection study, 2×10^5 cells were first harvested via dissociation with TrypLE Express (ThermoFisher Scientific) and then resuspended in degassed PBS containing calcium and magnesium (PBS+/+) for each sample. The TMBs were added to the cell suspension at a ratio of 15 s-TMBs or 7 l-TMBs per cell, and incubated for 40 minutes at RT on a rotator. Next, the cell binding to the MBs were observed using optical microscopy. Following incubation, pGFP (10 μg) was added, and degassed PBS+/+ was supplemented to a total volume of 200 μL to each sample. The samples were incubated at RT for another 40 minutes prior to the ultrasound treatment. For the flow cytometry, six groups were tested: 1) NTC, 2) pGFP with transfection reagent JetPrime (Polyplus), 3) pGFP + s-TMB, 4) pGFP + s-TMB + US, 5) pGFP + l-TMB, 6) pGFP + l-TMB + US. After ultrasound treatment, the samples were mixed for five more minutes at RT on a rotator. Following pGFP transfection, cells were cultured at 37 °C in a humidified 5% CO_2 incubator. Flow cytometry was conducted after 48 h. Cells were harvested in 500 μL of TrypLE Express, and viable cell number was calculated by using a hemocytometer, and trypan blue stained dead cells were excluded. The fraction of GFP^+ cells was measured via FACScan flow cytometer (BD Biosciences), and data were analyzed using FlowJo vX software (Tree Star). All treatments were analyzed in triplicate.

4.8 ELISA

For the pGM-CSF transfection study, 10^6 cells were firstly harvested via dissociation with TrypLE Express (ThermoFisher Scientific) and resuspended in degassed PBS containing calcium and magnesium (PBS+/+) for each sample. The TMBs were added to the cell suspension at a ratio of 15 s-TMBs or 7 l-TMBs per cell, and incubated for 40 min at room temperature (RT) on a rotator. Next, the cell binding to the MBs were observed using optical microscopy. Following the incubation, pGM-CSF (25 ug) was added, and degassed PBS+/+ was supplemented to a total volume of 200 μL to each sample. The samples were incubated at RT for another 40 min prior to the ultrasound treatment. For the ELISA study, six groups were tested: 1) NTC, 2) pGM-CSF with transfection reagent JetPrime (Polyplus Transfection) as positive control, 3) pGM-CSF + s-TMB, 4) pGM-CSF + s-TMB + US, 5) pGM-CSF + l-TMB, 6) pGM-CSF + l-TMB + US. After ultrasound treatment, the samples were mixed for 5 more minutes at RT on a rotator. GM-CSF production was assayed 48 h after treatment. Culture media was collected and centrifuged at 300 RCF for 10 minutes at 4°C. The supernatant without debris was transferred to a fresh tube, and GM-CSF content in undiluted samples was measured via ELISA (#ab201276, Abcam) following the manufacturer's instructions. The adherent cells were harvested by using cell scrapers, and the total protein in the cells was measured via BCA Protein Assay (Thermo Fisher Scientific). GM-CSF concentration was normalized to total protein for each sample. All treatments were analyzed in triplicate.

4.9 *In vivo* transfection studies

All animal-related work was in accordance with Guide for the Care and Use of Laboratory Animals of the National Institutes of Health [49], and all animal experiments were performed under a protocol approved by the Institutional Animal Care and Use Committee of Stanford University. All mice in this study were female FVB mice (6 weeks old, ~20 g; Charles River). Mice were orthotopically injected with NDL cells (1×10^6 cells/25 μL of PBS−/−) into the left inguinal mammary fat pad (#4). Transfection was started when tumors reached 3 to 4 mm in the average diameter (~10 days after cell injections). Prior to ultrasound treatment, the mice were shaved and fur further removed using a depilatory cream. Acoustic gel was used as a coupling agent. Anesthesia was induced with 2% isoflurane in oxygen (2 L/min). A mixture of 25 μg of pLuc with 2×10^7 s-TMBs or 10^7 l-TMBs (final injected volume of 25 μL) was freshly prepared before doing an intratumoral (i.t.) injection. The injection preceded sonication by 5 min to allow for MB diffusion in the TME and binding to the cells. The animal was positioned on its side above an agarose spacer with the tumor to receive the ultrasound treatment facing the 250 kHz transducer [12]. Intratumoral injection (i.t.) of a mixture of 25 μg of pLuc with 2×10^7 s-TMBs or 10^7 l-TMBs (final injected volume was 25 μL). Injected dose was freshly prepared and injected, and preceded sonication by 5 min for MB targeting. The TMB distribution and destruction during ultrasound treatment was assessed by real-time ultrasound imaging in contrast mode.

Two types of plasmids were used for the *in vivo* transfection studies: pLuc and pGFP. For pLuc transfection, four groups of mice were studied (n = 3): 1) PBS; 2) pLuc +US; 3) pLuc + s-TMB + US; 4) pLuc + l-TMB + US. After 24 h, the pLuc expression was visualized by living imaging in bioluminescence mode (Lago, Spectral Instruments Imaging). For pGFP transfection, three groups of mice were studied: 1) NTC (n=1), 2) pGFP + s-TMB +US (n = 4), 3) pGFP + l-TMB + US (n = 4). After 24 h, the pGFP expression in tumors was visualized by ex vivo imaging in fluorescence mode (Lago). GFP: Ex = 395 nm, Em = 509 nm.

4.10 *In vivo* histology study

Tumors from bilateral NDL (breast cancer) tumor-bearing mice were studied via histology. Mice were orthotopically injected with NDL cells (1 × 10^6 cells/25 μL of PBS−/−) into the bilateral #4 and #9 inguinal mammary fat pad. Therapy was started when tumors reached 3~4 mm in the average diameter (~10 d after cell injections). Prior to the ultrasound treatment, the mice were shaved and fur further removed using a depilatory cream. Acoustic gel was used as a coupling agent. Anesthesia was induced with 2% isoflurane in oxygen (2 L/min). A mixture of 25 μg of pGM-CSF with 2 × 10^7 s-TMBs or 10^7 l-TMBs (final injected volume of 25 μL) was freshly prepared before intratumoral (i.t.) injection. The animal was positioned on the side above an agarose spacer with one of the bilateral tumors facing the 250 kHz transducer [13]. For histology, pGM-CSF was administered, and seven groups of mice were studied (n=3, 6 tumors per group): 1) NTC, 2) aPD-1; 3) l-TMB + US; 4) pGM-CSF + l-TMB + US; 5) aPD-1 + l-TMB + US; 6) aPD-1 + pGM-CSF + s-TMB + US; 7) aPD-1 + pGM-CSF + l-TMB + US. In the regimen, 200 μg of aPD-1 was injected intraperitoneally (i.p.) on Day 1, and DNA vaccination and ultrasound treatment were executed on Day 4. On Day 7, both treated and distant tumors were dissected and fixed for 72 hours in 10% neutral buffered formalin before transferred to 70% ethanol. Hematoxylin and eosin (H&E) staining and immunohistochemistry (IHC) of CD8 and F4/80 biomarkers for tumor samples were processed by UC Davis Medical Center. The digital images of the staining slices were viewed using the ImageScope program (Leica Biosystems).

4.11 Anticancer efficacy study

For anticancer efficacy study, seven groups of mice were studied (n=3, 6 tumors per group): 1) NTC, 2) aPD-1; 3) l-TMB + US; 4) pGM-CSF + l-TMB + US; 5) aPD-1 + l-TMB + US; 6) aPD-1 + pGM-CSF + s-TMB + US; 7) aPD-1 + pGM-CSF + l-TMB + US. In the regimen, 200 μg of aPD-1 was injected intraperitoneally (i.p.) on Day 1 and Day 5, and DNA vaccination and ultrasound treatment were executed on Day 4 and Day 8. The tumor volumes and body weight of mice were measured and recorded every three days. On Day 35, both treated and distant tumors were dissected and fixed overnight in 10% neutral buffered formalin and transferred to 70% alcohol the next day. H&E staining and IHC of Ki67 biomarker for tumor samples were processed by UC Davis Medical Center. The digital images of staining slices were viewed using the ImageScope program (Leica Biosystems).

4.12 Statistical analysis

Statistical analyses were performed using GraphPad Prism 8 software. Results are presented as mean ± standard deviation, and all experiments were repeated at least 3 times. Analysis of differences between two normally distributed test groups was performed using an unpaired t test assuming unequal variance. For t tests comparing two groups, the mean of each treatment group was compared only to the mean of the control group and the Welch's t test with multiple comparisons correction was applied. Statistical tests are reported in the relevant captions. P values < 0.05 were considered significant and were adjusted for multiple comparisons as indicated in the legends.

Supplementary Material

Refer to Web version on PubMed Central for supplementary material.

Acknowledgments

This work was supported by National Institutes of Health Grants (R01CA112356 and R01CA227687), and China Scholarship Council (No. 201906010082).

Reference

1. Mellman I, Coukos G, and Dranoff G, Cancer immunotherapy comes of age. Nature, 2011. 480(7378): p. 480–9. [PubMed: 22193102]
2. Bonaventura P, et al. , Cold Tumors: A Therapeutic Challenge for Immunotherapy. Front Immunol, 2019. 10: p. 168. [PubMed: 30800125]
3. Ott PA, et al. , Combination immunotherapy: a road map. J Immunother Cancer, 2017. 5: p. 16. [PubMed: 28239469]
4. Banchereau J and Palucka K, Immunotherapy: Cancer vaccines on the move. Nat Rev Clin Oncol, 2018. 15(1): p. 9–10. [PubMed: 28895570]
5. Berraondo P, et al. , Cytokines in clinical cancer immunotherapy. Br J Cancer, 2019. 120(1): p. 6–15. [PubMed: 30413827]
6. Donnelly JJ, Wahren B, and Liu MA, DNA vaccines: progress and challenges. J Immunol, 2005. 175(2): p. 633–9. [PubMed: 16002657]
7. Anguela XM and High KA, Entering the Modern Era of Gene Therapy. Annual review of medicine, 2019. 70: p. 273–288.
8. Harrop R, John J, and Carroll MW, Recombinant viral vectors: cancer vaccines. Adv Drug Deliv Rev, 2006. 58(8): p. 931–47. [PubMed: 17030074]
9. Arbuthnot P, Viral Vectors for Delivery of Antiviral Sequences, in Gene Therapy for Viral Infections. 2015. p. 95–126.
10. Li SD and Huang L, Gene therapy progress and prospects: non-viral gene therapy by systemic delivery. Gene Ther, 2006. 13(18): p. 1313–9. [PubMed: 16953249]
11. Al-Dosari MS and Gao X, Nonviral gene delivery: principle, limitations, and recent progress. AAPS J, 2009. 11(4): p. 671–81. [PubMed: 19834816]
12. Ilovitsh T, et al. , Low-frequency ultrasound-mediated cytokine transfection enhances T cell recruitment at local and distant tumor sites. Proc Natl Acad Sci U S A, 2020.
13. Bez M, et al. , Nonviral ultrasound-mediated gene delivery in small and large animal models. Nat Protoc, 2019. 14(4): p. 1015–1026. [PubMed: 30804568]
14. Ferrara K, Pollard R, and Borden M, Ultrasound microbubble contrast agents: fundamentals and application to gene and drug delivery. Annu Rev Biomed Eng, 2007. 9: p. 415–47. [PubMed: 17651012]
15. Wrenn SP, et al. , Bursting bubbles and bilayers. Theranostics, 2012. 2(12): p. 1140–59. [PubMed: 23382772]
16. Collis J, et al. , Cavitation microstreaming and stress fields created by microbubbles. Ultrasonics, 2010. 50(2): p. 273–9. [PubMed: 19896683]
17. Lentacker I, et al. , Understanding ultrasound induced sonoporation: definitions and underlying mechanisms. Adv Drug Deliv Rev, 2014. 72: p. 49–64. [PubMed: 24270006]
18. Mullick Chowdhury S, Lee T, and Willmann JK, Ultrasound-guided drug delivery in cancer. Ultrasonography, 2017. 36(3): p. 171–184. [PubMed: 28607323]

19. Qin P, et al. , Mechanistic understanding the bioeffects of ultrasound-driven microbubbles to enhance macromolecule delivery. J Control Release, 2018. 272: p. 169–181. [PubMed: 29305924]
20. Li YS, et al. , Optimising ultrasound-mediated gene transfer (sonoporation) in vitro and prolonged expression of a transgene in vivo: potential applications for gene therapy of cancer. Cancer Lett, 2009. 273(1): p. 62–9. [PubMed: 18829156]
21. Kim MG, et al. , Investigation of Optimized Treatment Conditions for Acoustic-Transfection Technique for Intracellular Delivery of Macromolecules. Ultrasound Med Biol, 2018. 44(3): p. 622–634. [PubMed: 29284555]
22. Jeon S-Y, Yoon J-Y, and Jang C-M, Bubble Size and Bubble Concentration of a Microbubble Pump with Respect to Operating Conditions. Energies, 2018. 11(7).
23. Doinikov AA, Haac JF, and Dayton PA, Resonance frequencies of lipid-shelled microbubbles in the regime of nonlinear oscillations. Ultrasonics, 2009. 49(2): p. 263–8. [PubMed: 18977009]
24. Yang Sun DEK, Dayton Paul A., Ferrara Katherine W., High-Frequency Dynamics of Ultrasound Contrast Agents. IEEE transactions on ultrasonics, ferroelectrics, and frequency control, 2005. 52(11): p. 1981–1991.
25. Feshitan JA, et al. , Microbubble size isolation by differential centrifugation. J Colloid Interface Sci, 2009. 329(2): p. 316–24. [PubMed: 18950786]
26. Dranoff G, GM-CSF-based cancer vaccines. Immunological Reviews, 2002. 188: p. 147–154. [PubMed: 12445288]
27. Fleetwood AJ, et al. , GM-CSF- and M-CSF-dependent macrophage phenotypes display differential dependence on type I interferon signaling. J Leukoc Biol, 2009. 86(2): p. 411–21. [PubMed: 19406830]
28. Tian H, et al. , A novel cancer vaccine with the ability to simultaneously produce anti-PD-1 antibody and GM-CSF in cancer cells and enhance Th1-biased antitumor immunity. Signal Transduct Target Ther, 2016. 1: p. 16025. [PubMed: 29263903]
29. Herweijer H and Wolff JA, Progress and prospects: naked DNA gene transfer and therapy. Gene Ther, 2003. 10(6): p. 453–8. [PubMed: 12621449]
30. Walther W, et al. , Stability analysis for long-term storage of naked DNA: impact on nonviral in vivo gene transfer. Analytical Biochemistry, 2003. 318(2): p. 230–235. [PubMed: 12814626]
31. Forster JC, et al. , A review of the development of tumor vasculature and its effects on the tumor microenvironment. Hypoxia (Auckl), 2017. 5: p. 21–32. [PubMed: 28443291]
32. Marmottant P, et al. , A model for large amplitude oscillations of coated bubbles accounting for buckling and rupture. The Journal of the Acoustical Society of America, 2005. 118(6): p. 3499–3505.
33. Chomas JE, et al. , Threshold of fragmentation for ultrasonic contrast agents. J Biomed Opt, 2001. 6(2): p. 141–50. [PubMed: 11375723]
34. Wang M, et al. , Sonoporation-induced cell membrane permeabilization and cytoskeleton disassembly at varied acoustic and microbubble-cell parameters. Sci Rep, 2018. 8(1): p. 3885. [PubMed: 29497082]
35. Yang Y, et al. , Mechanisms underlying sonoporation: Interaction between microbubbles and cells. Ultrason Sonochem, 2020. 67: p. 105096. [PubMed: 32278246]
36. Dranoff Glenn, J. E, Lazenby Audrey, Golumbek Paul, Levitsky Hyam, Brose Katja, Jackson Valerie, Hamada Hirofumi, Pardoll Drew, Mulligan Richard C., Vaccination with irradiated tumor cells engineered to secrete murine granulocyte-macrophage colony-stimulating factor stimulates potent, specific, and long-lasting anti-tumor immunity. Proc Natl Acad Sci U S A, 1993. 90(8): p. 3539–3543. [PubMed: 8097319]
37. ter Haar G, Therapeutic applications of ultrasound. Prog Biophys Mol Biol, 2007. 93(1-3): p. 111–29. [PubMed: 16930682]
38. Yerushalmi Rinat, W. R, Ravdin Peter M, Hayes Malcolm M, Gelmon Karen A, Ki67 in breast cancer: prognostic and predictive potential. Lancet Oncology, 2010. 11: p. 174–83. [PubMed: 20152769]
39. Knudsen KB, et al. , In vivo toxicity of cationic micelles and liposomes. Nanomedicine, 2015. 11(2): p. 467–77. [PubMed: 25168934]

40. Shi Y, et al. , Granulocyte-macrophage colony-stimulating factor (GM-CSF) and T-cell responses: what we do and don't know. Cell Res, 2006. 16(2): p. 126–33. [PubMed: 16474424]
41. Li B, et al. , Anti-programmed death-1 synergizes with granulocyte macrophage colony-stimulating factor--secreting tumor cell immunotherapy providing therapeutic benefit to mice with established tumors. Clin Cancer Res, 2009. 15(5): p. 1623–34. [PubMed: 19208793]
42. Hu Y, Wan JM, and Yu AC, Cytomechanical perturbations during low-intensity ultrasound pulsing. Ultrasound Med Biol, 2014. 40(7): p. 1587–98. [PubMed: 24642219]
43. Kvåle S, et al. , Size fractionation of gas-filled microspheres by flotation. Separations Technology, 1996. 6(4): p. 219–226.
44. Batchelor GK and Green JT, The determination of the bulk stress in a suspension of spherical particles to order c 2. Journal of Fluid Mechanics, 2006. 56(03).
45. Lin HAO, Storey BD, and Szeri AJ, Inertially driven inhomogeneities in violently collapsing bubbles: the validity of the Rayleigh–Plesset equation. Journal of Fluid Mechanics, 2002. 452: p. 145–162.
46. Ilovitsh T, et al. , Enhanced microbubble contrast agent oscillation following 250 kHz insonation. Sci Rep, 2018. 8(1): p. 16347. [PubMed: 30397280]
47. Qin S and Ferrara KW, A model for the dynamics of ultrasound contrast agents in vivo. J Acoust Soc Am, 2010. 128(3): p. 1511–21. [PubMed: 20815486]
48. Miller JK, et al. , Suppression of the negative regulator LRIG1 contributes to ErbB2 overexpression in breast cancer. Cancer Res, 2008. 68(20): p. 8286–94. [PubMed: 18922900]
49. National Research Council, Guide for the Care and Use of Laboratory Animals. 8th ed. Committee for the Update of the Guide for the Care and Use of Laboratory Animals. 2011 The National Academies Press https://www.nap.edu/.

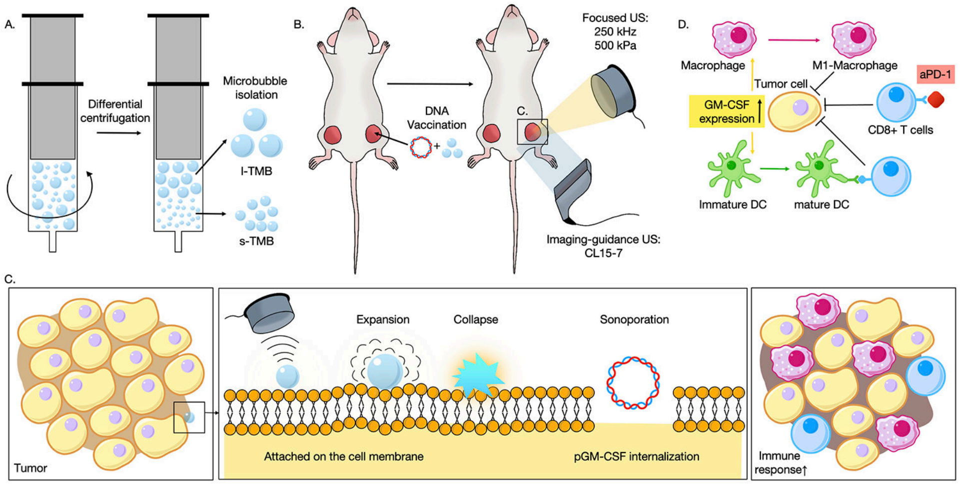

Figure 1.

Schematic illustration of the microbubble-based DNA transfection. A) Attributed to the extra hydrostatic pressure applied on the microbubbles, size-specific bubbles were isolated via differential centrifugation; B) DNA plasmids and size-specific TMBs were mixed and co-injected into one mouse tumor, and low-frequency ultrasound with a center frequency of 250 kHz was applied to the treated tumor. C) The MBs underwent cycles of expansion and compression, and were subsequently destroyed. The resulting sonoporation enhanced the internalization of pGM-CSF DNA plasmid. D) Next, pGM-CSF was translated and expressed and an immune response was initiated.

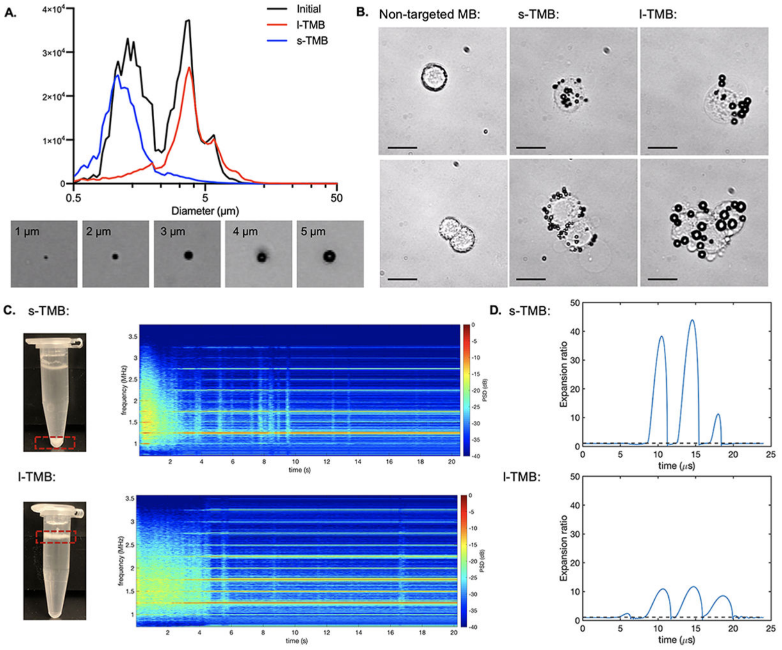

Figure 2.

A) Diameter distribution for pre-segmented TMBs, s-TMBs and l-TMBs, and representative images for 1, 2, 3, 4 and 5 μm TMBs under optical microscopy. B) Representative optical images of s-TMBs and l-TMBs adherent to cells and cell clusters. Scale bar: 30 μm. C) Spectrogram of the received signals from PCD as a function of time for s-TMBs and l-TMBs. D) Expansion ratio as a function of time for s-TMB (diameter= 1 μm) and l-TMB (diameter = 4 μm) simulated by using the Marmottant model.

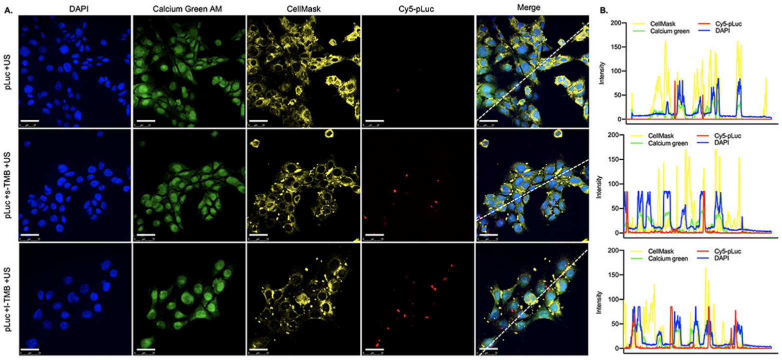

Figure 3.

A) Confocal laser microscopy images of cellular distribution of Cy5-pLuc after sonoporation with no TMB (top panel), s-TMBs (middle) and l-TMBs (bottom). Scale bars: 25 μm. B) Fluorescence intensities for each channel were quantified based on the dashed line in the microscopic images in Figure 3A.

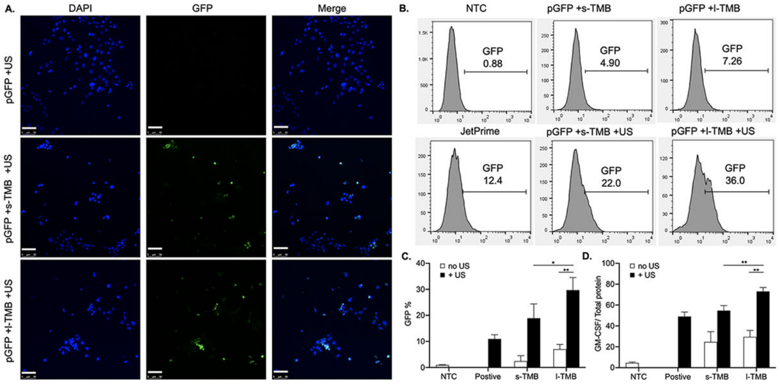

Figure 4.

A) Confocal microscopy images of GFP expression in TMB-treated cells and merged with DAPI for nuclear localization. B) Flow cytometry results for pGFP expression after 48 h and C) quantification of the percentage of GFP^+ cells in the treatment groups. D) ELISA results for GM-CSF production after 48 h. *P < 0.05 and **P < 0.01. All data are plotted as mean ± SD.

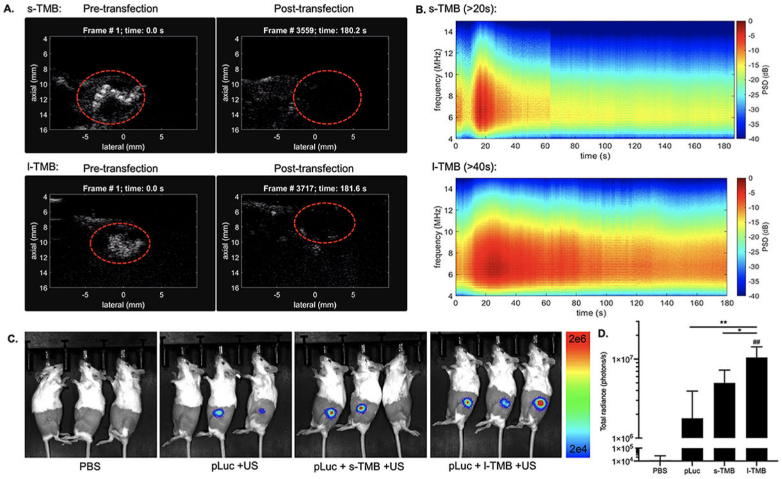

Figure 5.

A) Ultrasound real-time imaging in contrast mode showing TMB distribution in tumor during insonation. Images were captured at 0 s and after 3-min ultrasound application in s-TMB and l-TMB groups of mice. B) Spectrogram of the received signals of PCD in tumors as a function of time for s-TMBs and l-TMBs. C) Live optical imaging of mice and D) quantification of bioluminescence signals in tumors after 24 h. *P < 0.05, **P < 0.01 and ##P < 0.01 vs. NTC. All data are plotted as mean ± SD.

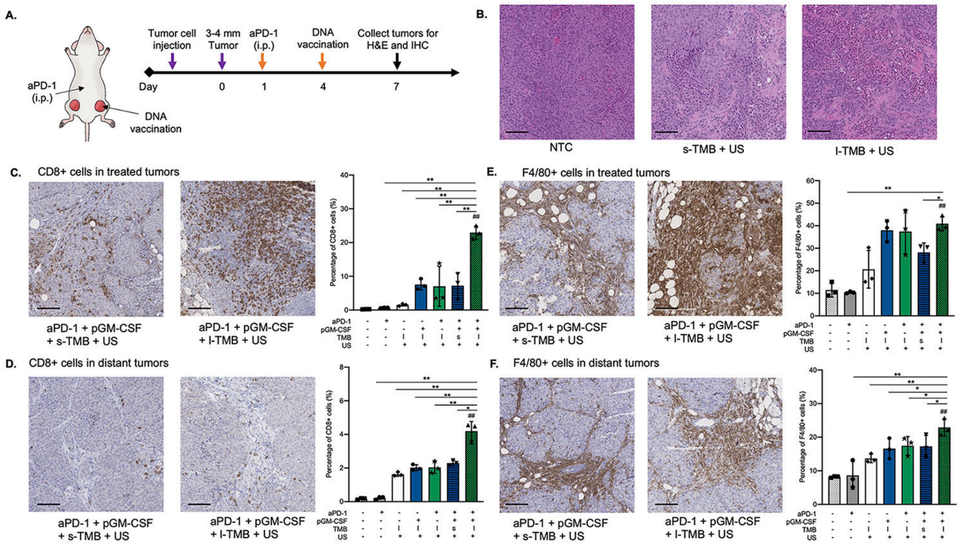

Figure 6.

A) Schematic illustration of the therapeutic regimen with DNA vaccination: aPD-1 was injected on Day 1, and the mixture of pGM-CSF and TMBs was co-injected into one tumor within the bilateral tumor model in mice, followed by ultrasound treatment on Day 4. B) H&E staining in NTC, s-TMB + US and l-TMB + US treated tumor samples. IHC staining of CD8 in C) treated tumors and D) distant tumors in different groups. IHC staining of F4/80 in E) treated tumors and F) distant tumors in different groups. (Scale bars: 100 μm). $^{*}P < 0.05$, $^{**}P < 0.01$ and $^{\#\#}P < 0.01$ vs. NTC. All data are plotted as mean ± SD.

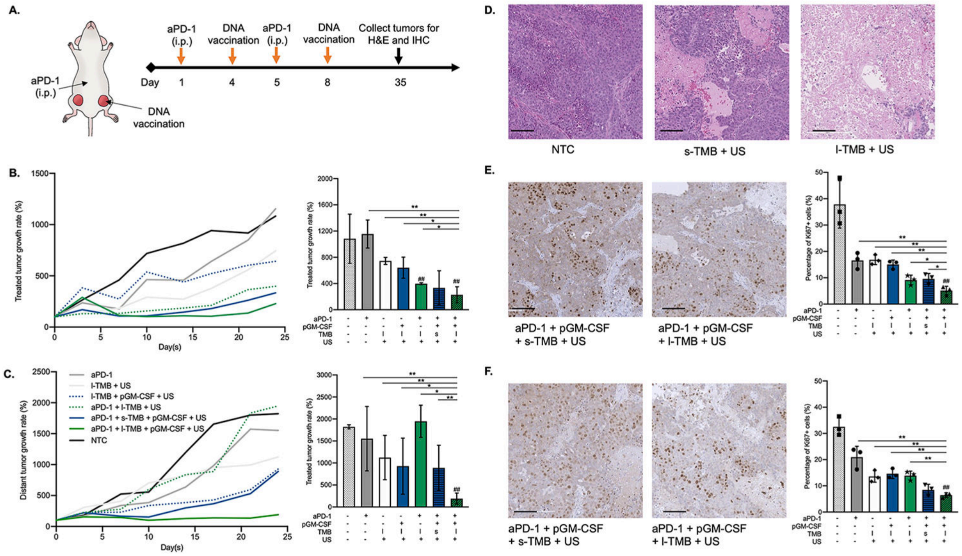

Figure 7.

A) Schematic illustration of the immunotherapy regimen: aPD-1 was injected on Day 1 and Day 5, and the mixture of pGM-CSF and TMB was co-injected into one tumor within the bilateral tumor model in mice, followed by ultrasound treatment on Day 4 and Day 8. Tumor growth and comparison of B) treated and C) distant tumors on Day 25. D) H&E staining in NTC, s-TMB + US and l-TMB + US treated tumor samples. IHC staining of Ki67 in E) treated and F) distant tumors. (Scale bars: 100 μm). *$P < 0.05$, **$P < 0.01$ and ##$P < 0.01$ vs. NTC. All data are plotted as mean ± SD.